



# CHORUS

This is the accepted manuscript made available via CHORUS. The article has been published as:

## Angle-resolved photoemission spectroscopy study of the Möbius Kondo insulator candidate CeRhSb

Seungho Seong, Kyoo Kim, Eunsook Lee, Chang-Jong Kang, Taesik Nam, B. I. Min, Takenobu Yoshino, T. Takabatake, J. D. Denlinger, and J.-S. Kang

Phys. Rev. B **100**, 035121 — Published 22 July 2019

DOI: [10.1103/PhysRevB.100.035121](https://doi.org/10.1103/PhysRevB.100.035121)

# Angle-resolved Photoemission Spectroscopy Study of the Möbius Kondo Insulator Candidate CeRhSb

Seungho Seong<sup>1,\*</sup>, Kyoo Kim<sup>2,3,\*</sup>, Eunsook Lee<sup>1</sup>, Chang-Jong Kang<sup>2,†</sup>, Taesik Nam<sup>2</sup>, B. I. Min<sup>2</sup>, Takenobu Yoshino<sup>4</sup>, T. Takabatake<sup>4</sup>, J. D. Denlinger<sup>5,‡</sup> and J.-S. Kang<sup>1,§</sup>

<sup>1</sup>*Department of Physics, The Catholic University of Korea, Bucheon 14662, Korea*

<sup>2</sup>*Department of Physics, Pohang University of Science and Technology, Pohang, 37673, Korea*

<sup>3</sup>*MPPHC-CPM, Pohang University of Science and Technology, Pohang 37673, Korea*

<sup>4</sup>*Department of Quantum Matter, Graduate School of Advanced Sciences of Matter, Hiroshima University, Higashi-Hiroshima 739-8530, Japan*

<sup>5</sup>*Advanced Light Source (ALS), Lawrence Berkeley Laboratory, Berkeley, CA. 12345, USA*

The electronic structure of a Möbius Kondo insulator (MKI) candidate of CeRhSb has been investigated by employing angle-resolved photoemission spectroscopy (ARPES), and the density functional theory (DFT) and dynamical mean-field theory (DMFT) band calculations. Fermi surfaces (FS's) and band structures are successfully measured for three orthogonal crystallographic directions. A sharp Ce 4*f* peak is observed at the Fermi level ( $E_F$ ), and its temperature ( $T$ )-evolution agrees with that of the Ce 4*f* Kondo resonance. The metallic FS's are obtained for all three different (100), (010), and (001) planes. The Ce 4*f* FS's are described properly by the unfolded DFT calculations considering the reduced Ce-only unit cell. The  $T$ -dependence of Ce 4*f* states as well as the dispersive coherent Ce 4*f* bands are described well by the DMFT calculations, and reveal the anisotropic  $c$ - $f$  hybridization. The photon energy dependence of the Fermi-edge states in CeRhSb reveals the 3*D* character, consistent with the bulk states dispersing to  $E_F$  over a larger energy scale rather than the predicted Möbius topological surface states.

PACS numbers: 79.60.-i, 71.20.-b, 71.27.+a, 71.20.Eh

## I. INTRODUCTION

Topological Kondo insulators (TKI's) belong to a class of the symmetry-protected topological phases arising from the effects of strong correlation.<sup>1,2</sup> In TKI's, the temperature ( $T$ )-dependent Kondo hybridization between conduction electrons and localized  $f$ -electrons leads to the formation of a narrow gap in the bulk bands at the Fermi level ( $E_F$ ) and the topologically non-trivial band inversion. The first theoretically-predicted TKI was SmB<sub>6</sub>,<sup>1,2</sup> which was known as a mixed-valent (Sm<sup>2+</sup>/Sm<sup>3+</sup>) Kondo insulator, but having the resistivity saturation at low  $T$ . The metallic surface states have been observed by angle-resolved photoemission spectroscopy (ARPES)<sup>3-6</sup> and transport experiment,<sup>7-10</sup> supporting SmB<sub>6</sub> being a promising candidate for a TKI. But there are conflicting ARPES reports, claiming SmB<sub>6</sub> being just a trivial Kondo insulator.<sup>11,12</sup> Subsequently, other rare-earth  $f$ -electron systems, such as YbB<sub>6</sub>, YbB<sub>12</sub>, and  $g$ -SmS, were proposed as TKI's or topological Kondo semi-metals.<sup>13-17</sup> Nevertheless, the general consensus on the 4*f*-electron TKI's is still lacking.<sup>18</sup>

It has been recently predicted that CeNiSn, CeRhSb, and CeIrSb are novel topological Kondo systems having Möbius-twisted surface states.<sup>19</sup> They belong to the failed Kondo insulators, for which an insulating gap develops due to the Kondo screening and yet a semi-metallic phase is stabilized at lower  $T$ , exhibiting large anisotropy.<sup>20-22</sup> The  $f$ -electron pseudo gaps of size 15–20 meV were observed at  $E_F$  in high-resolution PES for CeRhSb<sup>23,24</sup> with a metallic density of states (DOS) at  $E_F$ , supporting a Kondo semi-metallic phase. On the

other hand, tiny gaps as small as  $\sim 28$  K ( $\sim 2.3$  meV) and  $\sim 7$  K ( $\sim 0.6$  meV) were reported in NMR<sup>25</sup> and in resistivity experiments,<sup>26</sup> respectively.

The unique features of these systems are the non-symmorphic glide and screw axis symmetries ( $Pnma$  space group) (see Fig. 1), which bring about the hourglass-type new topological surface band structures.<sup>19</sup> Hence these systems are called the Möbius Kondo Insulators (MKI's). But the predicted features of the MKI's have not been confirmed experimentally yet.

In this work, we have studied the electronic structures of a candidate MKI, CeRhSb, employing both ARPES experiment and the density functional theory (DFT) and dynamical mean-field theory (DMFT) band calculations. We have successfully measured Fermi surfaces (FS's) and band structures for the three orthogonal crystallographic directions. This is important because theoretically the Möbius surface states are predicted only for the (010) surface, while the (100) surface is predicted to be insulating.<sup>19</sup> We have also performed  $T$ -dependent ARPES measurement, and observed significant broadening in the Ce 4*f* peak near  $E_F$ , which allows us to estimate the coherence temperature,  $T_{coh}$ , of Ce 4*f* states.

## II. EXPERIMENTAL AND CALCULATIONAL DETAILS

Single-crystalline CeRhSb samples were prepared by the Bridgman method.<sup>22</sup> They were characterized to be of very good quality and exhibited strong anisotropy in thermal conductivity. The details of the sample prepara-

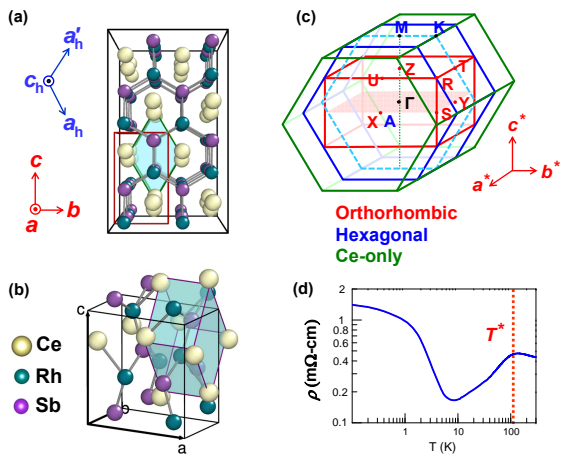


FIG. 1: (Color online) Crystal structure and BZ of CeRhSb. (a) The orthorhombic  $\epsilon$ -TiNiSi-type structure viewed from the [100] direction, showing that the orthorhombic structure is slightly deformed from the hexagonal structure. (b) The original unit cell (black lines) versus the reduced Ce-only unit cell (the blue-colored cell), for which only Ce ions are considered and Rh and Sb ions are ignored. (c) The BZ's of the orthorhombic (red), hexagonal (blue), and Ce-only (green) structures, superposed onto one another. (d) The resistivity  $\rho(T)$  for polycrystalline CeRhSb (adapted from Ref. <sup>38</sup>).

tion and characterization are described in Ref. <sup>[22]</sup>. According to the X-ray analysis, the lattice constants are  $a=7.47$  Å,  $b=4.63$  Å, and  $c=7.89$  Å.

ARPES measurements were carried out at the MERLIN beamline 4.0.3 at the Advanced Light Source (ALS) synchrotron. Single crystalline samples were cleaved *in situ* using a blade-type cleaver, <sup>27</sup> and measured in vacuum better than  $5 \times 10^{-11}$  Torr and at  $T \sim 20$  K with further cooling to 6 K during  $T$ -dependent measurements. Fermi level ( $E_F$ ) energy referencing was performed with evaporated gold. A total energy resolution of  $\Delta E \approx 25$  meV was employed at 122 eV photon energy, <sup>27</sup> and the detector  $0.1^\circ$  angular resolution translates to momentum resolution of  $\Delta k < 0.01$  Å<sup>-1</sup> at 122 eV. FS maps were obtained via polar scans of the sample. In plotting FS maps, the energy window of  $E_i \pm 16$  meV was integrated. <sup>28</sup> Photon energies corresponding to the high-symmetry planes were determined from the photon energy ( $h\nu$ ) scans. <sup>29</sup>

We have calculated the electronic structure of CeRhSb within the DFT using the full-potential local-orbital band method (FPLO) in the generalized-gradient approximation. <sup>30</sup> To describe the band structures in an effectively reduced unit cell, we have utilized the band unfolding scheme <sup>31</sup> implemented in the FPLO code. To describe the strong electron correlation effect of the Ce 4*f* state in the Kondo coherence regime, we have utilized the DFT+DMFT method implemented in the Wien2k code. <sup>32,33</sup> One-crossing approximation (OCA) was used for the DMFT impurity solver. <sup>34</sup> The on-site Coulomb  $U=5.5$  eV and Hund's coupling  $J=0.68$  eV for the Ce 4*f* electrons were adopted in the DMFT calculation.

Figure 1(a) shows a view from the [100] direction in the  $\epsilon$ -TiNiSi-type orthorhombic structure of CeRhSb. <sup>35</sup> CeRhSb has an AlB<sub>2</sub>-derivative structure (Al=Ce, B=Rh, Sb) having a subcell with Rh and Sb atoms on the hexagons. <sup>36</sup> The orthorhombic structure of CeRhSb is slightly deformed from the hexagonal structure, for which the  $a$ -axis in the orthorhombic structure corresponds to the  $c_h$ -axis in the hexagonal structure. <sup>37</sup> Ce atoms form a zigzag chain along  $a$  ( $c_h$ ). <sup>37</sup> Hence large anisotropic physical properties are expected to originate from the Ce chains along  $a$  (along  $c_h$  in the hexagonal structure) in CeRhSb, in agreement with the reported properties. <sup>20-22</sup> Figures 1(b) and (c) show the original versus the Ce-only reduced unit cells, and the Brillouin zones (BZ's) of the orthorhombic, hexagonal, and Ce-only structures, superposed onto one other, respectively. The  $\Gamma$ - $X$ ,  $\Gamma$ - $Z$ , and  $\Gamma$ - $Y$  lines in the orthorhombic BZ are along the  $\Gamma$ - $A$ ,  $\Gamma$ - $M$ , and  $\Gamma$ - $K$  lines in the hexagonal BZ.

Figure 1(d) shows the resistivity  $\rho(T)$  for polycrystalline CeRhSb, reproduced from Ref. <sup>38</sup>. It exhibits a typical  $\rho(T)$  behavior of a Kondo insulator, having a hump and dip structure at  $T^* \sim 100 - 150$  K and  $T \approx 10$  K, respectively. <sup>16</sup> At very low  $T$ , it shows a hint of the plateau-like behavior. A similar behavior was observed in Ref. <sup>26</sup>

### III. RESULTS AND DISCUSSION

The Kondo-like temperature evolution of the  $f$ -states in CeRhSb along  $\bar{X}\bar{\Gamma}\bar{X}$  for the (001) surface is presented in Fig. 2, measured at the Ce 4*f* resonance ( $h\nu=122$  eV) using linear horizontal (LH) polarization. The ARPES images for selected temperatures of this data set are shown in Fig. 2(a), exhibiting two separated strong Fermi-edge peaks on either side of normal emission ( $\bar{\Gamma}$ ). This feature at low  $T$  is expected to reflect the dispersive nature of Ce 4*f* band. With increasing  $T$ , the  $f$ -amplitudes decrease and the peaks broaden gradually until they are not resolved. This trend agrees with the  $T$ -dependent behavior of the calculated DMFT band structures shown in Fig. 2(b). This behavior is highlighted by plotting the Fermi-edge momentum distribution curves (MDC) both as an image in Fig. 2(c) and as the line cuts in Fig. 2(d). The  $T$ -dependent variation of the Fermi-edge states manifests that, upon heating, the sharp peaks broaden into a broad hump at  $T^* \sim 100$  K, indicating that the coherent Ce 4*f* band along  $\bar{\Gamma}$ - $\bar{X}$  disappears above  $\sim 100$  K, suggesting  $T_{coh} \approx T^* \approx 100$  K. Figure 2(e) shows the full  $T$ -series of the angle-integrated energy distribution curve (EDC) spectra, which highlights the energy, width, and amplitude variation of the resonantly enhanced  $f$ -character Kondo peak near  $E_F$ . The additional broad feature at  $-0.3$  eV represents a final-state spin-orbit (SO) side band peak. With increasing  $T$ , the intensity of the Kondo peak decreases dramatically with the concomitant broadening of its energy width.

The  $T$ -dependent variations of the DMFT band struc-

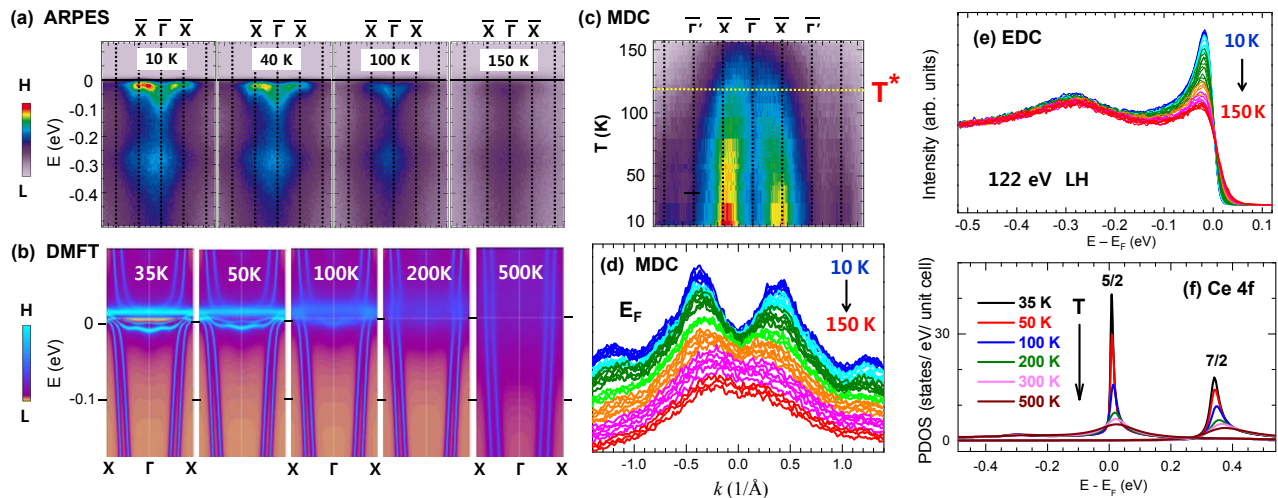


FIG. 2: (Color online)  $T$ -dependent  $4f$  states of CeRhSb. All the ARPES data were obtained at the Ce  $4f$  resonance ( $h\nu=122$  eV). (a) The ARPES images along  $\bar{X}\bar{\Gamma}\bar{X}$  for selected temperatures. (b) The calculated  $T$ -dependent DMFT band structures. (c) The MDC images of the Fermi-edge states along  $\bar{X}\bar{\Gamma}\bar{X}$  from 10 K to 150 K. (d) The  $E_F$ -intensity profile of the MDC's along  $\bar{X}\bar{\Gamma}\bar{X}$  from 10 K to 150 K. (e) The angle-integrated energy distribution curve (EDC) spectra from 10 K to 150 K. (f) The calculated  $T$ -dependent variation of the Ce  $4f$  PDOS, obtained in the DMFT.

ture and the Ce  $4f$  partial density of states (PDOS) are shown in Figs. 2(b) and (f), respectively. Upon cooling below  $T \approx 100$  K, the Ce  $4f$  Kondo-resonance band near  $E_F$  and the flat SO side bands at  $\sim \pm 0.3$  eV are formed (see Fig. 8 in the Appendix), in agreement with the measured ARPES data. In fact, this  $T$ -evolution behavior of CeRhSb both in ARPES and DMFT is consistent with its  $\rho(T)$  behavior, having a maximum at  $T^* \approx 100$  K (see also Fig. 1(a)).<sup>26,38</sup>

Figures 3(a)-(c) show the measured FS's and ARPES spectra, obtained at the Ce  $4f$  resonance, and the DFT-calculated FS's of CeRhSb for three different planes. The FS's in the top panel reveal clearly the six-fold symmetry for the (100) plane, the nearly four-fold symmetry for the (010) plane, and the two-fold symmetry for the (001) plane. The observed FS for the (100) plane supports the relation between the orthorhombic and hexagonal structures, described in Fig. 1. These FS's reflect that all (100), (010), (001) surfaces are metallic. The (100) plane exhibits the circular FS's around  $\Gamma$  points of the hexagonal BZ, while the (010) plane exhibits rather large elliptical FS's and the (001) plane reveals the complicated FS's of polka-dot patterns. Unlike the theoretical prediction,<sup>19</sup> no gap is quantified in the (100) plane in our ARPES.

The FS's and ARPES bands in Fig. 3(a)-(c) arise from the Kondo resonance states. The measured FS's in the (010) plane are larger than the size of the orthorhombic BZ, but appear to fit in with the enlarged BZ's, implying the reduced unit cell. This strange feature arises from the fact that these FS's originate from Ce  $4f$  electrons. Indeed, such a reduced unit cell can be obtained when considering Ce atoms only but ignoring Rh and Sb atoms (see Fig. 1 and Fig. 6). Since the FS's in Fig. 3(a)-(c)

were obtained at the Ce resonance, they are dominated by Ce  $4f$  electrons, and the contributions from Rh  $4d$  and Sb  $5p$  electrons are negligibly weak.<sup>40</sup> This interpretation is supported by the smaller sizes of the FS, obtained at  $h\nu=108$  eV away from the Ce  $4f$  resonance (see Fig. 3(d)-(f)), in which the Rh  $4d$  electron contribution is large.

The measured Ce  $4f$  states along  $\bar{X}\bar{\Gamma}\bar{X}$  in the (001) plane (in Fig. 3(c)) show the hole-like FS pockets around  $\bar{X}$  and an electron-like pocket around  $\bar{\Gamma}$ . They are more dispersive than those along  $M\bar{\Gamma}M$  in Fig. 3(a) and along  $\bar{Z}\bar{\Gamma}\bar{Z}$  in Fig. 3(b).<sup>29</sup> The dispersive Ce  $4f$  states along  $\bar{X}\bar{\Gamma}\bar{X}$  originate from the zigzag Ce chain along  $[100]$ . In fact, the DMFT calculation at  $T=50$  K also shows the almost coherent Ce  $4f$  band at  $E_F$ , revealing the formation of the hybridization gap. The DMFT band structures of CeRhSb in the whole BZ, given in Fig. 8 in the Appendix, show the coherent Ce  $4f$  Kondo-resonance band near  $E_F$  and the flat SO side bands at around  $\pm 0.3$  eV. The observed band slopes indicate the larger effective mass along  $M\bar{\Gamma}M$  and  $\bar{Z}\bar{\Gamma}\bar{Z}$ , while a smaller effective mass along  $\bar{X}\bar{\Gamma}\bar{X}$ . Such differences reflect the anisotropic  $c$ - $f$  hybridization ( $c$ : conduction electron) along different  $k$  directions, in agreement with the observed anisotropic properties.<sup>20,22</sup>

The DFT-calculated FS's in the middle panel of Figs. 3(a)-(c) represent those unfolded into the larger BZ of the reduced Ce-only unit cell (see Fig. 6 and Fig. 7 in the Appendix). It is noteworthy that the low- $T$  electronic structures and their FS's of strongly-correlated  $f$ -electron systems are simulated well by the renormalized DFT bands.<sup>16,34</sup> Indeed, the comparison between the measured FS's and the calculated FS's reveals fairly good agreement. Especially, the FS for the (100) plane in Fig. 3(a), exhibiting the hexagonal-like symmetry, is

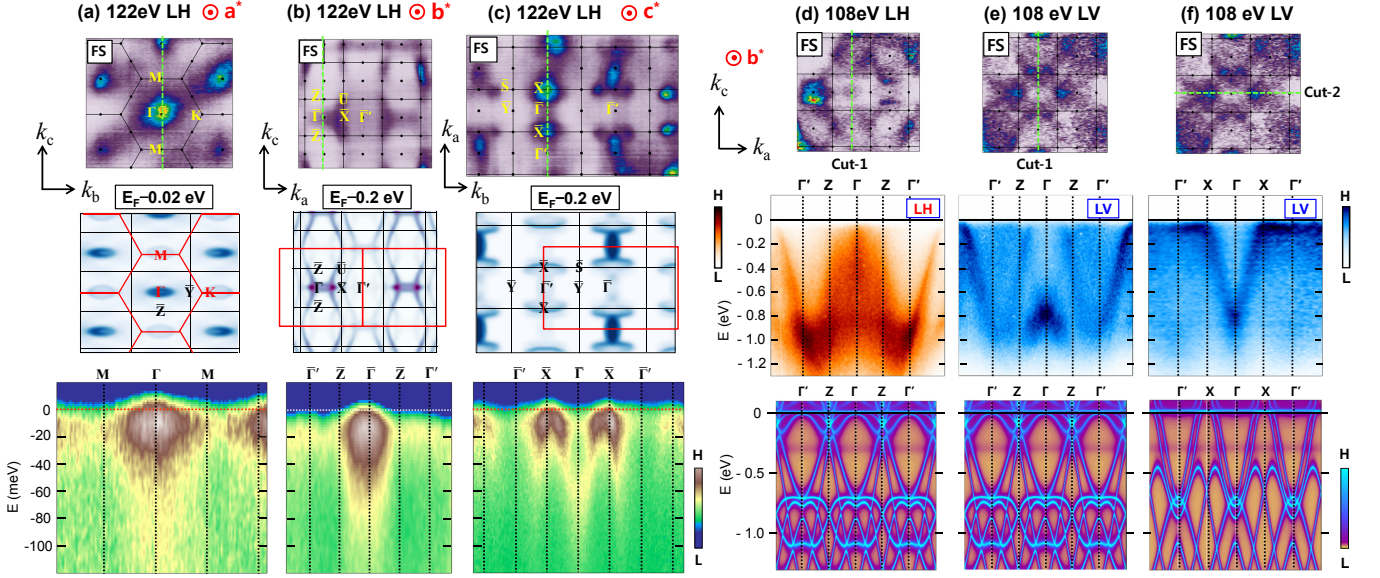


FIG. 3: (Color online) (a)-(c) Fermi surfaces (FS's) and ARPES data obtained at the Ce 4*f* resonance ( $h\nu=122$  eV)<sup>29</sup> and at  $T=20$  K with the LH polarization, and the DFT-calculated FS's of CeRhSb for three orthogonal planes, respectively. In the top panel are shown the measured FS's for the (100) plane, the (010) plane, and the (001) plane, respectively. The middle panel presents the DFT-calculated FS's,<sup>39</sup> which are unfolded into a larger hexagonal BZ (in red) of the Ce-only unit cell. The original orthorhombic BZ's are denoted in black. In the bottom panel are shown the measured ARPES spectra along the several cuts, denoted as green dotted lines in the FS's of top panel. (d)-(f) FS's and ARPESs of CeRhSb for the (010) plane obtained at  $T=20$  K with  $h\nu=108$  eV,<sup>29</sup> and the corresponding DMFT band structures calculated at  $T=50$  K. (d) ARPES along  $\Gamma'Z\Gamma Z\Gamma'$  (Cut-1) (denoted as green dotted lines in the FS of top panel), obtained with the LH-polarization, is compared with the DMFT band structure at the bottom. (e),(f) Similarly for two ARPESs along  $\Gamma'Z\Gamma Z\Gamma'$  (Cut-1) and along  $\Gamma'X\Gamma X\Gamma'$  (Cut-2), respectively, both of which are obtained with the LV-polarization.

described fairly well by the FS unfolded into the larger hexagonal BZ (in red) of Ce-only unit cell. Further, the spectral weights of the FS's for the (010) and (001) planes (in Figs. 3(b) and (c)) match well with the periodicity of the Ce-only BZ, as shown in the middle panels.

Figures 3(d)-(f) show the comparison between the measured ARPES data, obtained with  $h\nu=108$  eV,<sup>29</sup> and the DMFT bands calculated at  $T=50$  K for CeRhSb. Note that, in the 108 eV ARPES data, Rh 4*d* states are observed. In Fig. 3(d) are compared the ARPES image plot along  $\Gamma'Z\Gamma Z\Gamma'$ , obtained with the LH polarization, with the DMFT-calculated bands along the same direction. Similarly, the ARPES image plots along  $\Gamma'Z\Gamma Z\Gamma'$  and  $\Gamma'X\Gamma X\Gamma'$ , obtained with the linear-vertical (LV)-polarized photons, are compared with the corresponding DMFT-calculated bands in Figs. 3(e) and (f), respectively. Excluding the flat Ce 4*f* states in DMFT, they reveal reasonably good agreement. Both the shapes and energy positions of the measured Rh bands agree well with those in the calculated DMFT.<sup>41</sup>

In order to check whether the metallic states, observed in our ARPES, have the 2*D* topological surface-state (TSS) character, we have measured the  $h\nu$ -dependence of the Fermi-edge states for CeRhSb (called the  $h\nu$ -map hereafter). Figures 4(a) and (b) show the Fermi-edge state  $h\nu$ -map, obtained between 30 eV and 118 eV with

$h\nu$  along  $k_b$ , and that between 100 eV and 150 eV with  $h\nu$  along  $k_c$ , respectively. The  $h\nu$  map in the  $k_b$ - $k_c$  plane exhibits the elliptical FS's and the roughly two-fold symmetry, while that in the  $k_a$ - $k_c$  plane exhibits the hole-like FS's<sup>43</sup> around  $U$  points, providing evidence for the 3*D* character of the Fermi-edge states in CeRhSb. Namely, the theoretically predicted TSS's of the 2*D* character<sup>19</sup> are not observed. This finding does not rule out the possible MKI of CeRhSb, because it may be due to the lack of the ARPES energy resolution relative to the small gap size. Nevertheless, the 3*D* character of the metallic states observed in Fig. 4 indicates that only the pseudo gap opens in CeRhSb, with the gap size  $\lesssim 20$  meV, which is consistent with the earlier high-resolution PES<sup>23,24</sup> and tunneling studies.<sup>21</sup> Therefore, this work suggests that a crucial factor for the realization of the existence of the TSS in a potential MKI is the full bulk insulating energy gap on top of the non-symmorphic crystal symmetries. In this respect, the isostructural CeRhAs, which possesses the full bulk energy gap, would be more appropriate to explore the TSS of MKI.

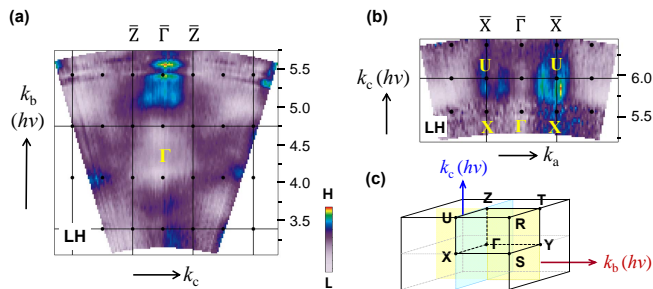


FIG. 4: (Color online) The Fermi-edge state  $h\nu$ -maps, (a) between 30 eV and 118 eV with  $h\nu$  along  $k_b$ , and (b) between 100 eV and 150 eV with  $h\nu$  along  $k_c$ . Both are obtained with the LH-polarization. (c) The 3D orthorhombic BZ for which  $h\nu$ -maps are obtained: the  $k_c$ - $k_b$  (yellow) and  $k_a$ - $k_c$  (blue) planes for (a) and (b), respectively.

#### IV. CONCLUSIONS

In conclusion, we have successfully measured the FS's and band structures of an MKI candidate CeRhSb for the three orthogonal crystallographic directions. A sharp Ce 4*f* peak is observed at  $E_F$  and its  $T$ -evolution agrees with that of the coherent Ce 4*f* band formation, suggesting  $T_{coh} \approx 100$  K. The metallic FS's are obtained for all three different (100), (010), and (001) planes. The Ce 4*f* FS's are described very well by the unfolded DFT calculations considering the reduced Ce-only unit cell. The  $T$ -dependence of Ce 4*f* states as well as the dispersive coherent Ce 4*f* bands are described well by the DMFT calculations, and reveal the anisotropic  $c$ - $f$  hybridization. The  $h\nu$ -dependences of the Fermi-edge states reveal their 3D metallic character, which is consistent with the bulk states dispersing to  $E_F$  over a larger energy scale rather than the TSS's over the tiny hybridization gap. To make a firm realization of the existence of the TSS's of the MKI, the ultralow- $T$  and very high-resolution ARPES experiment at the state-of-the-art ARPES beamline is highly desirable.<sup>44,45</sup> Such an experiment is quite challenging, in particular for CeRhSb, because of the intrinsic limitation due to the non-ideally flat surfaces of the cleaved samples.<sup>27</sup>

**Acknowledgments** – This work was supported by the National Research Foundation (NRF) of Korea (No. 2019R1A2C1004929; No. 2017M2A2A6A01071297; No. 2017R1A2B4005175), Max-Planck POSTECH/KOREA Research Initiative (No. 2016K1A4A4A01922028), and KISTI (Grant No. KSC-2017-C3-0057). The ALS is supported by US DOE under Contract No. DE-AC02-05CH11231. The travel for the ARPES experiment at the ALS was supported in part by MSIP and PAL in Korea.

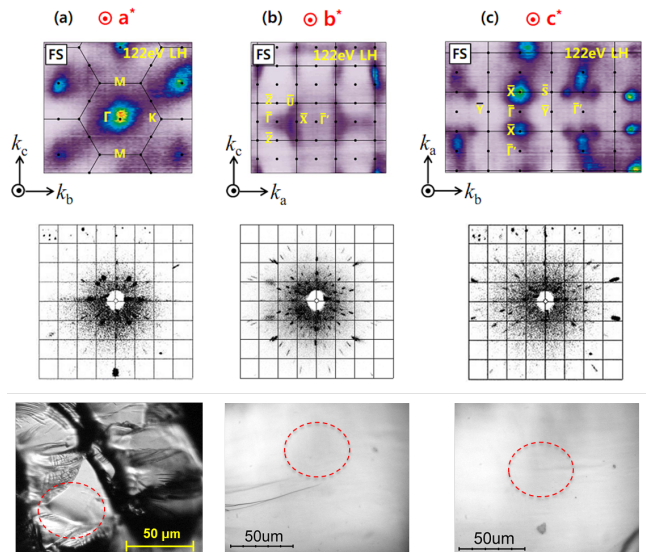


FIG. 5: (Color online) Fermi surface (FS) maps, Laue patterns, and optical microscopy (OM) images for CeRhSb for three different planes. (a) The measured FS and Laue pattern for the (100) plane (perpendicular to the  $a$ -axis, and  $k_b$ - $k_c$  plane) At the bottom is shown the OM image of the cleaved surface, taken after the ARPES measurement. (b), (c) Similarly for the (010) plane (the plane perpendicular to the  $b$  axis;  $k_a$ - $k_c$  plane) and for the (001) plane (the plane perpendicular to the  $c$  axis;  $k_a$ - $k_b$  plane), respectively. Red-colored dotted lines in the OM images at the bottom panels denote the beam sizes for the ARPES measurement.

#### V. APPENDIX

Figure 5 shows the measured FS's, the Laue patterns, and the optical microscopy (OM) images for CeRhSb for three different planes. The Laue patterns (middle panel) and the OM images (bottom panel) were obtained from the corresponding cleaved surfaces for which ARPES measurements were done. The OM images reveal that the ARPES data presented in this paper were obtained from the flat regions because the beam size employed in ARPES measurements was less than  $\lesssim 60 \times 50 \mu\text{m}$ . Both FS and Laue data reveal clearly the six-fold symmetry for the (100) plane, the nearly four-fold symmetry for the (010) plane, and the two-fold symmetry for the (001) plane, respectively. These symmetries support the relation between the orthorhombic and hexagonal crystal structures, described in the text. These FS and Laue data confirm that we have obtained three different cleaved planes of CeRhSb properly, and that the ARPES data presented in this paper represent those for the (100), (010), and (001) planes. As shown at the bottom of Fig. 5, the cleaved surfaces were flat and large enough for ARPES measurements, but they were not perfectly flat, suggesting that the energy resolution of the ARPES data is limited by the non-ideally-flat surfaces. Hence, even ultra-high resolution and ultra-low  $T$  ARPES would have to overcome this limit in order to observe the topo-

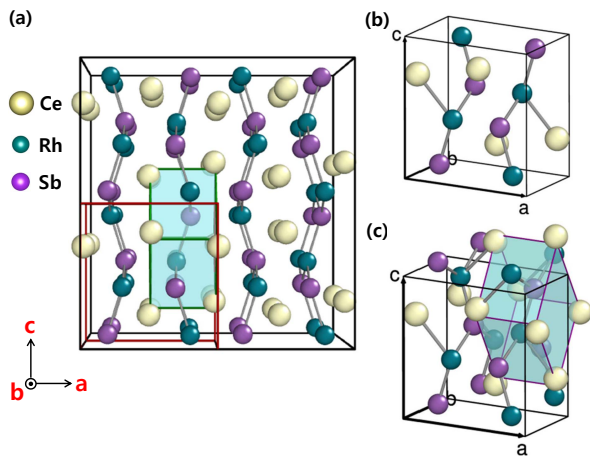


FIG. 6: (Color online) Unfolding procedure of the “Ce-only” unit cell. (a) The orthorhombic  $\epsilon$ -TiNiSi-type structure viewed from the [010] direction (from the  $b$  axis). Yellow, green, and violet balls denote Ce, Rh, and Sb atoms, respectively. (b) The unit cell in the orthorhombic structure. (c) The “Ce-only” unit cell, for which only Ce ions are considered and Rh and Sb ions are ignored.

logical metallic surface states inside the very small energy gap ( $\lesssim$  a few meV).

The “Ce-only unfolding” scheme is shown in Fig. 6. The orthorhombic  $\epsilon$ -TiNiSi-type structure, viewed from the [010] direction (from the  $b$  axis) is shown in Fig. 6(a), and its unit cell is shown in Fig. 6(b). Figure 6(c) compares the unit cell of the orthorhombic structure (black lines) and the “Ce-only” unit cell (purple lines), where only Ce atoms are considered but Rh and Sb ions are ignored. This figure shows that, if only Ce atoms are considered and Rh and Sb ions are ignored, the corresponding “Ce-only” unit cell becomes reduced from the original orthorhombic unit cell under the following relation:

$$\begin{bmatrix} \tilde{a} \\ \tilde{b} \\ \tilde{c} \end{bmatrix} = \begin{bmatrix} 2 & 0 & 0 \\ 0 & 1 & -1 \\ 0 & 1 & 1 \end{bmatrix} \begin{bmatrix} a \\ b \\ c \end{bmatrix}.$$

Here  $a$ ,  $b$ ,  $c$  denote the lattice axes of the original orthorhombic unit cell, and  $\tilde{a}$ ,  $\tilde{b}$ ,  $\tilde{c}$  denote the lattice axes of the “Ce-only” unit cell. There are four Ce atoms in the original unit cell, while there is only one Ce atom in the “Ce-only” unit cell. Then the Brillouin zone (BZ) for the “Ce-only” unit cell becomes enlarged and rotated from the original orthorhombic BZ accordingly, under the following relation between two BZ’s:

$$\begin{bmatrix} \tilde{a}^* \\ \tilde{b}^* \\ \tilde{c}^* \end{bmatrix} = \begin{bmatrix} 1 & 0 & 0 \\ 0 & 1 & -1 \\ 0 & 1 & 1 \end{bmatrix} \begin{bmatrix} a^* \\ b^* \\ c^* \end{bmatrix}.$$

Here  $a^*$ ,  $b^*$ ,  $c^*$  denote the axes of the BZ for the original orthorhombic unit cell, and  $\tilde{a}^*$ ,  $\tilde{b}^*$ ,  $\tilde{c}^*$  denote the axes of the BZ for the “Ce-only” unit cell. Note that the

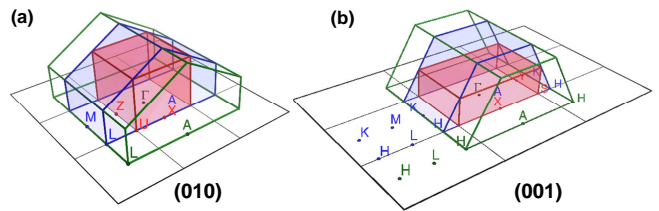


FIG. 7: (Color online) (a) Schematic drawings of the hexagonal (red) and the Ce-only (green) BZ’s on top of the (010) orthorhombic BZ. (b) Similarly for the (001) orthorhombic BZ.

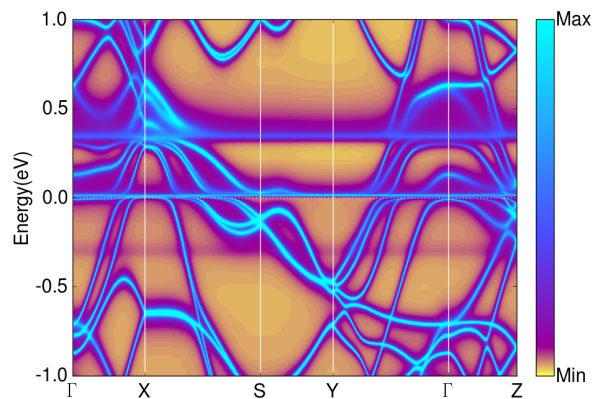


FIG. 8: (Color online) Dynamical mean-field theory (DMFT) band structure of CeRhSb at  $T=50$  K. The Coulomb correlation  $U=5.5$  eV and the exchange correlation  $J=0.68$  eV were used in the DMFT calculations, and the one-crossing approximation (OCA) was used for the DMFT impurity solver.

positions of Rh and Sb atoms are exchanged to each other in the next “Ce-only” unit cell (see Fig. 6(c)). We think that this is the situation for our FS and ARPES data obtained with  $h\nu = 122$  eV (Ce  $4f$  resonance).

Figure 7 depicts the hexagonal and Ce-only BZ’s on top of the (010) and the (001) orthorhombic BZ’s, corresponding to Fig. 3(b) and Fig. 3(c) in the main text, respectively. Note that the Ce-only BZ is twice larger than the hexagonal BZ along the orthorhombic  $a^*$  direction, giving rise to the intensity modulation with the periodicity of  $2 \times a^*$ . Note that the spectral weights of the Fermi surfaces match well with the periodicity of the Ce-only BZ (see Figs. 3(b) and (c) in the main text).

Figure 8 shows the dynamical mean-field theory (DMFT) band structure of CeRhSb calculated at  $T=50$  K for the whole BZ. The coherent Ce  $4f$  Kondo-resonance band near  $E_F$  and the flat SO side bands at around  $\pm 0.3$

eV are observed, in agreement with the measured ARPES data (see Fig. 2). The SO side band above  $E_F$  is more

pronounced than that below  $E_F$ .

- 
- \* Co-first authors: They contributed equally.  
<sup>†</sup> Present address: Department of Physics and Astronomy, Rutgers University, Piscataway, New Jersey, 08854, USA  
<sup>‡</sup> Co-corresponding: [JDDenlinger@lbl.gov](mailto:JDDenlinger@lbl.gov)  
<sup>§</sup> Co-corresponding: [kangjs@catholic.ac.kr](mailto:kangjs@catholic.ac.kr)
- <sup>1</sup> M. Dzero, K. Sun, V. Galitski, and P. Coleman, *Phys. Rev. Lett.* **104**, 106408 (2010).
  - <sup>2</sup> M. Dzero, K. Sun, P. Coleman, and V. Galitski, *Phys. Rev. B* **85**, 045130 (2012).
  - <sup>3</sup> M. Neupane, N. Alidoust, S.-Y. Xu, T. Kondo, Y. Ishida, D. J. Kim, Chang Liu, I. Belopolski, Y. J. Jo, T.-R. Chang, H.-T. Jeng, T. Durakiewicz, L. Balicas, H. Lin, A. Bansil, S. Shin, Z. Fisk, and M. Z. Hasan, *Nature Commun.* **4**, 3991 (2013).
  - <sup>4</sup> N. Xu, X. Shi, P. K. Biswas, C. E. Matt, R. S. Dhaka, Y. Huang, N. C. Plumb, M. Radović, J. H. Dil, E. Pomjakushina, K. Conder, A. Amato, Z. Salman, D. McK. Paul, J. Mesot, H. Ding, and M. Shi, *Phys. Rev. B* **88**, 121102(R) (2013).
  - <sup>5</sup> J. Jiang, S. Li, T. Zhang, Z. Sun, F. Chen, Z. R. Ye, M. Xu, Q. Q. Ge, S. Y. Tan, X. H. Niu, M. Xia, B. P. Xie, Y. F. Li, X. H. Chen, H. H. Wen, and D. L. Feng *Nature Commun.* **4**, 4010 (2013).
  - <sup>6</sup> J. D. Denlinger, J. W. Allen, J.-S. Kang, K. Sun, J.-W. Kim, J. H. Shim, B. I. Min, Dae-Jeong Kim, Z. Fisk, arXiv: 1312.6637 (2013).
  - <sup>7</sup> S. Wolgast, C. Kurdak, K. Sun, J. W. Allen, D.-J. Kim, and Z. Fisk, *Phys. Rev. B* **88**, 180405(R) (2013).
  - <sup>8</sup> D. J. Kim, S. Thomas, T. Grant, J. Botimer, Z. Fisk, and Jing Xia, *Sci. Rep.* **3**, 3150 (2013).
  - <sup>9</sup> D. J. Kim, J. Xia, and Z. Fisk, *Nature Mater.* **13**, 466 (2014).
  - <sup>10</sup> S. Thomas, D. J. Kim, S. B. Chung, T. Grant, Z. Fisk, and Jing Xia, arXiv: 1307.4133 (2013).
  - <sup>11</sup> Z.-H. Zhu, A. Nicolaou, G. Levy, N. P. Butch, P. Syers, X. F. Wang, J. Paglione, G. A. Sawatzky, I. S. Elfimov, and A. Damascelli, *Phys. Rev. Lett.* **111**, 216402 (2013).
  - <sup>12</sup> P. Hlawenka, K. Siemensmeyer, E. Weschke, A. Varykhalov, J. Sánchez-Barriga, N. Y. Shitsevalova, A. V. Dukhnenko, V. B. Filipov, S. Gabáni, K. Flachbart, O. Rader, and E. D. L. Rienks, *Nat. Commun.* **9**, 517 (2018).
  - <sup>13</sup> B. Yan, L. Muchler, X.-L. Qi, S.-C. Zhang, and C. Felser, *Phys. Rev. B* **85**, 165125 (2012).
  - <sup>14</sup> X. Zhang, H. Zhang, J. Wang, C. Felser, S.-C. Zhang, *Science* **335**, 1464 (2012).
  - <sup>15</sup> Z. Li, J. Li, P. Blaha, and N. Kioussis, *Phys. Rev. B* **89**, 121117(R) (2014).
  - <sup>16</sup> C.-J. Kang, H. C. Choi, K. Kim, and B. I. Min, *Phys. Rev. Lett.* **114**, 166404 (2015).
  - <sup>17</sup> D. Kasinathan, K. Köpfernik, L. H. Tjeng, and M. W. Haverkort, *Phys. Rev. B* **91**, 195127 (2015).
  - <sup>18</sup> C.-J. Kang, J. D. Denlinger, J. W. Allen, C.-H. Min, F. Reinert, B. Y. Kang, B. K. Cho, J.-S. Kang, J. H. Shim, and B. I. Min, *Phys. Rev. Lett.* **116**, 116401 (2016).
  - <sup>19</sup> P.-Y. Chang, O. Erten, and P. Coleman, *Nature Phys.* **13**, 794 (2017); arXiv: 1603.03435v1.
  - <sup>20</sup> T. Takabatake, H. Tanaka, Y. Bando, H. Fujii, S. Nishigori, T. Suzuki, T. Fujita, and G. Kido, *Phys. Rev. B* **50**, 623 (1994).
  - <sup>21</sup> T. Ekino, T. Takabatake, H. Tanaka, and H. Fujii, *Phys. Rev. Lett.* **75**, 4262 (1995).
  - <sup>22</sup> M. Sera, N. Kobayashi, T. Yoshino, K. Kobayashi, T. Takabatake, G. Nakamoto, and H. Fujii, *Phys. Rev. B* **55**, 6421 (1997).
  - <sup>23</sup> H. Kumigashira, T. Takahashi, S. Yoshii, and M. Kasaya, *Phys. Rev. Lett.* **87**, 067206 (2001).
  - <sup>24</sup> K. Shimada, K. Kobayashi, T. Narimura, P. Baltzer, H. Namatame, M. Taniguchi, T. Suemitsu, T. Sasakawa, and T. Takabatake, *Phys. Rev. B* **66**, 155202 (2002).
  - <sup>25</sup> Y. Kawasaki, M. Izumi, Y. Kishimoto, T. Ohno, H. Tou, Y. Inaoka, M. Sera, and K. Shigetoh, and T. Takabatake, *Phys. Rev. B* **75**, 094410 (2007).
  - <sup>26</sup> T. Hiraoka, E. Kinoshita, H. Tanaka, T. Takabatake, H. Fujii, *J. Magn. Magn. Mater.* **153**, 124 (1996).
  - <sup>27</sup> As shown in Fig. 5 in the Appendix, the cleaved surfaces were not perfectly flat. Such non-ideally-flat surfaces can limit the energy resolution of the measured ARPES data.
  - <sup>28</sup> J. D. Denlinger, J. W. Allen, J.-S. Kang, K. Sun, B. I. Min, D.-J. Kim, and Z. Fisk, *J. Phys. Soc. Jpn. Conf. Proc.* **3**, 017038 (2014).
  - <sup>29</sup> For  $h\nu$  along [100],  $h\nu=122$  eV turns out to be close to the  $\Gamma Y T Z$  plane in the orthorhombic BZ, and  $\Gamma K M$  plane in the hexagonal BZ. For  $h\nu$  along [010],  $h\nu=108$  eV is close to the  $\Gamma Z U X$  plane in the orthorhombic BZ.
  - <sup>30</sup> K. Köpfernik and H. Eschrig, *Phys. Rev. B* **59**, 1743 (1999).; I. Opahle, K. Köpfernik, and H. Eschrig, *Phys. Rev. B* **60**, 14035 (1999).; H. Eschrig, K. Köpfernik, and I. Chaplygin, *J. Solid State Chemistry* **176**, 482 (2003).
  - <sup>31</sup> W. Ku, T. Berlijn, and C.-C. Lee, *Phys. Rev. Lett.* **104**, 216401 (2010).
  - <sup>32</sup> P. Blaha, K. Schwarz, G. K. H. Madsen, D. Kvasnicka, J. Luitz, WIEN2k, *An Augmented Plane Wave + Local Orbitals Program for Calculating Crystal Properties*, Karlheinz Schwarz, Techn. Universität Wien, Austria, (2001), ISBN 3-9501031-1-2.
  - <sup>33</sup> K. Haule, C.-H. Yee, and K. Kim, *Phys. Rev. B* **81**, 195107 (2010).
  - <sup>34</sup> H. C. Choi, B. I. Min, J. H. Shim, K. Haule, and G. Kotliar, *Phys. Rev. Lett.* **108**, 016402 (2012).
  - <sup>35</sup> F. Ishii and T. Oguchi, *J. Phys. Soc. Jpn.* **73**, 145 (2004).
  - <sup>36</sup> R. Pöttgen, O. Janka, and B. Chevalier, *Z. Naturforsch* **71**, 165 (2016).
  - <sup>37</sup> Indeed a similar compound of CeRhAs exhibits the structural transition from the hexagonal to orthorhombic structure below  $T=360$  K. See T. Sasakawa, K. Mine, K. Shigetoh, and T. Takabatake, *J. Phys. Soc. Jpn.* **74**, 3329 (2005).
  - <sup>38</sup> T. Takabatake, G. Nakamoto, H. Tanaka, Y. Bando, H. Fujii, S. Nishigori, H. Goshima, T. Suzuki, T. Fujita, I. Oguro, T. Hiraoka, and S. K. Malik, *Physica B* **199-200**, 462 (1994).
  - <sup>39</sup> In the calculated FS's, slightly deeper initial-state energies ( $E_i$ 's) are used instead of  $E_F$  ( $E_i \equiv 0$ ). This is because the shapes of the FS's and those of the constant-energy (CE) surfaces at slightly deeper  $E_i$ 's are very similar to

one another, but the latter exhibit clearer features than the former.

<sup>40</sup> J. J. Yeh and I. Lindau, *Atomic Data and Nuclear Data* **32**, 1 (1985).

<sup>41</sup> At present, the effect of the band unfolding is not implemented in the DMFT calculations. Hence the different ARPES intensities between the first and second BZ's are not elucidated in the DMFT bands in Figs. 3(d)-(f).

<sup>42</sup> The BZ's superposed on the  $h\nu$  maps are calculated by assuming the inner potential  $V_0=12$  eV.

<sup>43</sup> The hole-like character of the FS around  $U$  points in the  $k_a$ - $k_c$  plane (Fig. 4(b)) is confirmed by the photon-energy

dependence of the ARPES spectra. Unpublished data (Seunggho Seong, *et al.* (2018)).

<sup>44</sup> S. V. Borisenko, D. V. Evtushinsky, Z.-H. Liu, I. Morozov, R. Kappenberger, S. Wurmehl, B. Büchner, A. N. Yaresko, T. K. Kim, M. Hoesch, T. Wolf and N. D. Zhigadlo, *Nature Phys.* **12**, 311 (2013).

<sup>45</sup> Shouvik Chatterjee, Jan Trinckauf, Torben Hänke, Daniel E. Shai, John W. Harter, Travis J. Williams, Graeme M. Luke, Kyle M. Shen, and Jochen Geck, *Phys. Rev. Lett.* **110**, 186401 (2013).